Case Studies in Construction Materials 18 (2023) e02121

Contents lists available at ScienceDirect

Case Studies in Construction Materials

journal homepage: www.elsevier.com/locate/cscm

Identification and analysis of seashells in sea sand using computer vision and machine learning

Tiejun Liu [a], Yutong Ju [a], Hanxiong Lyu [a], Qinglin Zhuo [a], Hanjie Qian [b,*], Ye Li [a,*]

[a] School of Civil and Environmental Engineering, Harbin Institute of Technology, Shenzhen 518055, PR China
[b] School of Electrical and Electronic Engineering, Nanyang Technological University, Singapore 639798, Singapore

ARTICLE INFO

Keywords:
Sea sand
Seashell
Machine learning
Computer vision
Segmentation

ABSTRACT

Due to the shortage and high price of river sand, the use of sea sand as a fine aggregate for concrete is gradually being considered. Seashells are fragile and have an undesirable effect on the compressive strength of concrete. However, the exact effect of seashells is still unclear and quality control of concrete is not possible since there are no effective methods for seashell characterization. In this study, we investigated the feasibility of segmenting photos of sea sand and analyzing seashells by using three typical machine learning methods, i.e., PointRend, DeepLab v3 + , and Weka. A new imaging method was proposed to avoid overlapping sea sand particles and preserve the smallest particles with sufficient resolution. A total of 960 photos were captured, and 2199 seashells were labeled, of which 80% and 20% were used for model training and validation, respectively. As a result, PointRend could efficiently recognize seashells with different shapes, sizes, and surface textures. It also had the highest Intersection over Union (IOU) and pixel accuracy (PA) scores due to the well-defined boundaries of the seashells, followed by DeepLab v3 + and Weka. From the segmentation results, the size of the seashells showed a left-skewed distribution with a mean diameter of 0.747 mm, which was smaller than the size of the sea sand. There was also considerable variation in the irregularity and roundness of the seashells. As the size of the seashells increased, their shapes became more irregular. The automated analysis of the seashells can provide further insights into the effect of shells on the properties of concrete.

1. Introduction

Concrete production consumes large amounts of fresh water and river sand [1]. However, over-extraction of riverbed sand causes various problems such as loss of soil water retention capacity, sliding of river banks, lowering the water table, and destruction of river and lake ecosystems [2]. On the other hand, resources of sea sand are abundant. Therefore, the use of sea sand as a fine aggregate in concrete manufacturing is gradually being considered, especially in coastal regions [3,4].

Since sea sand is widely distributed, its physical and chemical properties vary significantly from place to place [5]. The incorporation of ions and impurities significantly changes the mechanical properties and durability of sea sand concrete [6–8]. X-ray diffraction (XRD) results show that the mineral compositions of sea sand and river sand are similar [9]. However, the compressive strength of sea sand concrete is lower than that of normal concrete due to the high content of fragile seashells and organic matter [10–12]. Therefore, thorough quality control is required when using sea sand in concrete. The identification and characterization of

* Corresponding authors.
E-mail addresses: hanjie001@e.ntu.edu.sg (H. Qian), liye@hit.edu.cn (Y. Li).

https://doi.org/10.1016/j.cscm.2023.e02121
Received 22 March 2023; Received in revised form 20 April 2023; Accepted 4 May 2023
Available online 4 May 2023
2214-5095/© 2023 Published by Elsevier Ltd. This is an open access article under the CC BY-NC-ND license (http://creativecommons.org/licenses/by-nc-nd/4.0/).

seashells in sea sands is a critical task. However, techniques such as loss on ignition (LOI), hydrochloric acid washing, and XRD can only roughly estimate total amount of seashells. A reliable and simple method for the quantitative identification of shells in sea sand has not yet been established. There are methods of counting particles from photographs, but they are very tedious and time-consuming to identify individual shell particles.

Conventional techniques such as edge detection, clustering, and thresholding are difficult to distinguish seashells from sea sand due to their similar features. Recent developments in machine learning and computer vision have made significant achievements in visual recognition [13]. Semantic segmentation algorithms based on deep learning have significantly improved the precision and processing speed of image segmentation. Such techniques have been widely used in various fields such as autonomous driving [14,15], medical imaging [16,17], face recognition [18,19] and geographic information systems [20]. Among them, convolutional neural networks (CNNs) were emphasized due to their overwhelming superiority in accuracy and efficiency. Researchers in the field of civil engineering have also noticed the advantages of deep learning. CNNs have been used to detect civil infrastructure defects such as cracks, spalling, and exposure of steel reinforcements [21,22]. Cha et al. introduced the application of CNN in crack identification [23]. Jang et al. proposed a deep learning–based autonomous concrete crack detection technique using hybrid images [24]. Park et al. applied YOLO in the crack localization in their paper [25]. Moreover, CNNs were also be applied on the analysis of concrete materials. A CNN model was proposed for predicting creep modulus of cement paste based on microstructure of concrete [26]. A new pathway was provided to extract representative features from back-scattered electron (BSE) images of ordinary Portland cement (OPC) and graphene oxide–silica reinforced OPC by using CNN [27]. Qian et al. classified concrete samples based on BSE images of concrete and CNN [28]. CNN was also used to conduct concrete segmentation analysis [29,30] and further to measure air voids in concrete without the use of color treatment [31].

Given the fruitful results obtained by employing deep learning in many fields, the work proposed in this paper aims to facilitate deep learning techniques to segment and quantify shells in sea sand. First, the sea sand was divided into three size ranges and photographed with a camera designed to be at an appropriate distance from the samples. Second, one machine learning algorithm (Weka segmentation) and two deep learning algorithms (PointRend and DeepLab v3 +) were adopted to segment the shells. Then, the performance of these segmentations was evaluated using Intersection over Union (IOU), pixel accuracy (PA), and average precision (AP) based on both training and test sets. Furthermore, the percentage of shells calculated based on image analysis was compared to the percentage of weight measured by the experimental LOI method. Finally, the size distribution and shape of the shells was calculated based on the shell masks.

2. Methodology

As shown in Section 2.1, we photographed the sea sand, labeled the shells, and constructed a database for training and testing. In Section 2.2, we describe the configuration of the three algorithms adopted and the process of training the models. Section 2.3 describes the method of measuring the weight percentage of the shells using LOI, and Section 2.4 describes the method of calculating the particle size distribution of the shells.

2.1. Image acquisition and dataset construction

Sea sands come in a wide range of particle sizes. To ensure that small sand and seashell particles have similar resolution and clarity as larger sand particles, sand samples were divided into three groups by sieving (0.6–1.25 mm, 1.25–2.5 mm, and 2.5–5.0 mm). The sands over 5 mm were excluded due to negligible weight percentages (less than 1.3% of the overall sample). The names SS (small sand), MS (middle sand), and LS (large sand) were used to indicate these three sample categories.

The sand particles were evenly adhered with black plaster during the shooting to avoid overlaying (Fig. 1). Meanwhile, the black

Fig. 1. Example for photo taking and cropping.

plaster serves as a high contrast background against the bright sand and shells. The photos of the sand particles were captured with a Canon@ 80D camera and an EF 100 mm f/2.8 L IS USM lens. This camera has a 6000 × 4000-pixel complementary metal-oxide-semiconductor sensor (CMOS). During the shooting, the distance between the camera and the sand sample was adjusted so that the width of the CMOS was 30 times the maximum sand size for each group. As a result, the pixel resolutions of the three sand groups were 6.25 μm/pixel, 12.5 μm/pixel, and 25 μm/pixel, respectively, confirming the similar distribution on the photographs even though the sand sizes were different.

A total of 960 pictures were taken, of which 320 belonged to each group. They were mixed in a ratio of 4:1 and randomly selected to form the training and test sets. After collection, each image was manually labeled by LableMe, as shown in Fig. 2. The regions of the shells were annotated one after another from the background. Here regions of interest are also called instances, and the organization of the dataset is shown in Table 1.

2.2. Configuration of network and algorithms

Distinguishing regions of seashells from sea sand particles and background can be considered a segmentation task in computer vision. In this study, three algorithms (PointRend [32], DeepLab v3 + [33], and Trainable Weka Segmentation [34]) were used.

The PointRend method is a deep learning module for image segmentation tasks that treats segmentation as an image rendering problem. This method achieves good segmentation performance on image test benchmarks. Furthermore, it is an end-to-end network that can automatically extract features without relying on manual features. The PointRend network is composed of the following main components:

Feature extractor: PointRend uses ResNet50 as the feature extraction part, extracting multi-scale feature maps from the input image. Then, a feature pyramid network (FPN) is used to fuse the feature maps of different scales into a unified 14 × 14 feature map, which serves as the input for subsequent processing.

ROI extraction: PointRend adopts the idea from Faster R-CNN, using an FPN network to generate ROIs (Region of Interest). For each generated ROI, PointRend predicts four heads: a class classifier for predicting the object category of the ROI, a box predictor for generating a bounding box around the object, a coarse mask classifier for generating an initial mask from the ROI's features, and a mask point classifier for generating points with the highest uncertainty in the mask, which will be recalculated to generate a more refined mask.

Mask rendering: PointRend uses a rendering strategy that divides the mask predictor into a coarse mask predictor and a mask point predictor. The coarse mask predictor generates an initial mask, and then the mask point classifier re-calculates the points with the highest uncertainty in the mask to refine the mask. This process results in a more detailed and accurate mask.

These components work together to enable PointRend to perform efficient end-to-end feature extraction, ROI extraction, and mask rendering in image segmentation tasks, leading to outstanding segmentation performance.(Fig. 3).

The DeepLab configuration is a variant of the FCN network [35] that performs well in semantic segmentation. One of the challenges of FCNs is that image details are lost while traversing through the convolutional and pooling layers of the network, resulting in fuzzy object boundaries. DeepLab v3 + uses an improved Atrous Spatial Pyramid Pooling (ASPP) module for image semantic segmentation to identify more explicit object boundaries [36]. The ASPP module applies convolutional operations by employing parallel Atrous convolutions at various rates to capture multi-scale contextual information. The results of DeepLab v3 are refined by the effective decoder module of DeepLab v3 + [33], which gradually recovers spatial information to capture sharper object boundaries. Fig. 4 shows the model structure used in this paper.

Trainable Weka Segmentation (TWS) is a machine learning tool for feature-based segmentation (Fig. 5). TWS converts the segmentation problem into a pixel level classification problem. First, input pixels were manually labeled into three classes (shell, sand,

Fig. 2. Example for labelling of seashells in the image.

Table 1
Organization of dataset.

	Training set	Validation set	Total
Number of images	768	192	960
Number of shells labeled	1773	426	2199

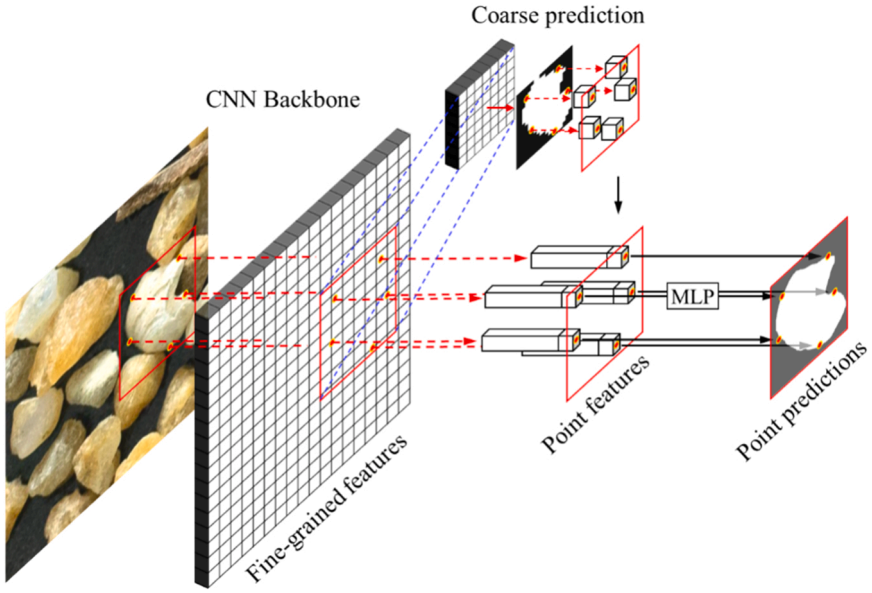

Fig. 3. Configuration of PointRend for seashell segmentation.

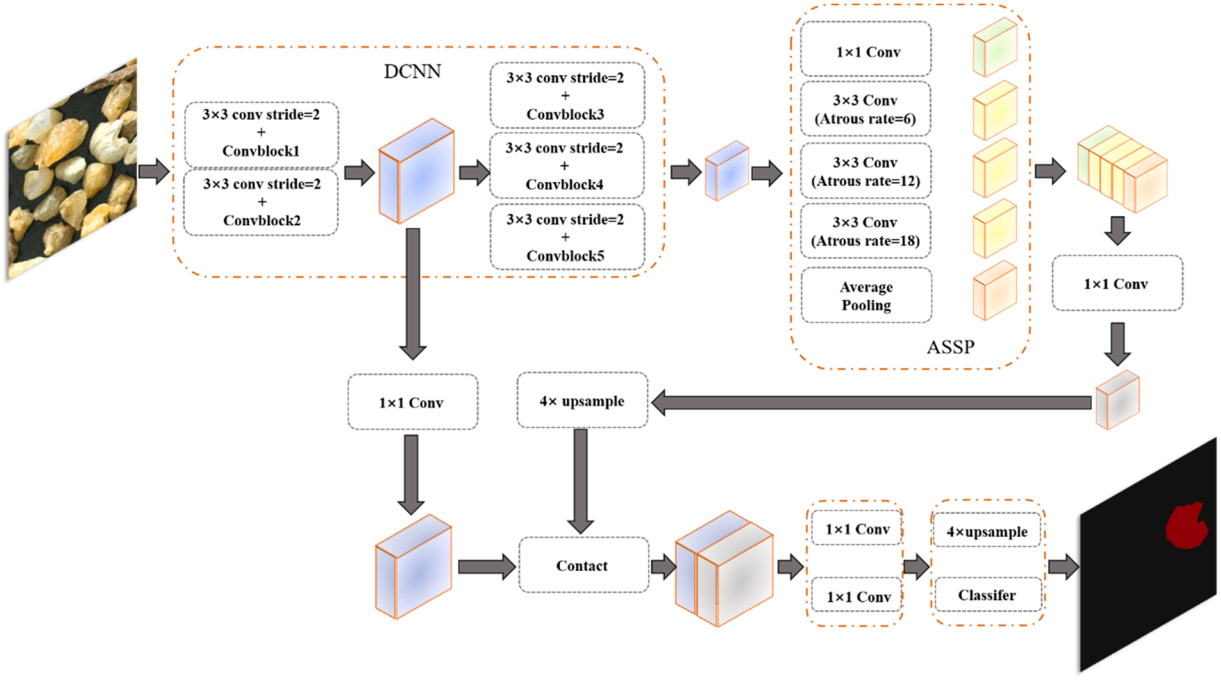

Fig. 4. Configuration of the DeepLabV3 for seashell segmentation.

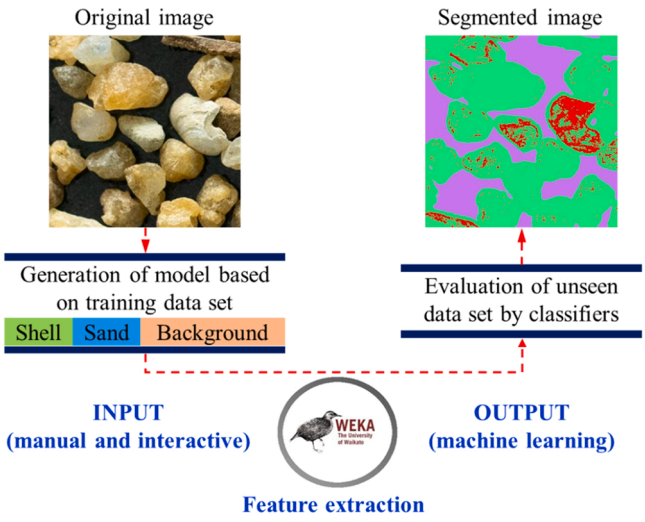

Fig. 5. TWS pipeline for seashell segmentation.

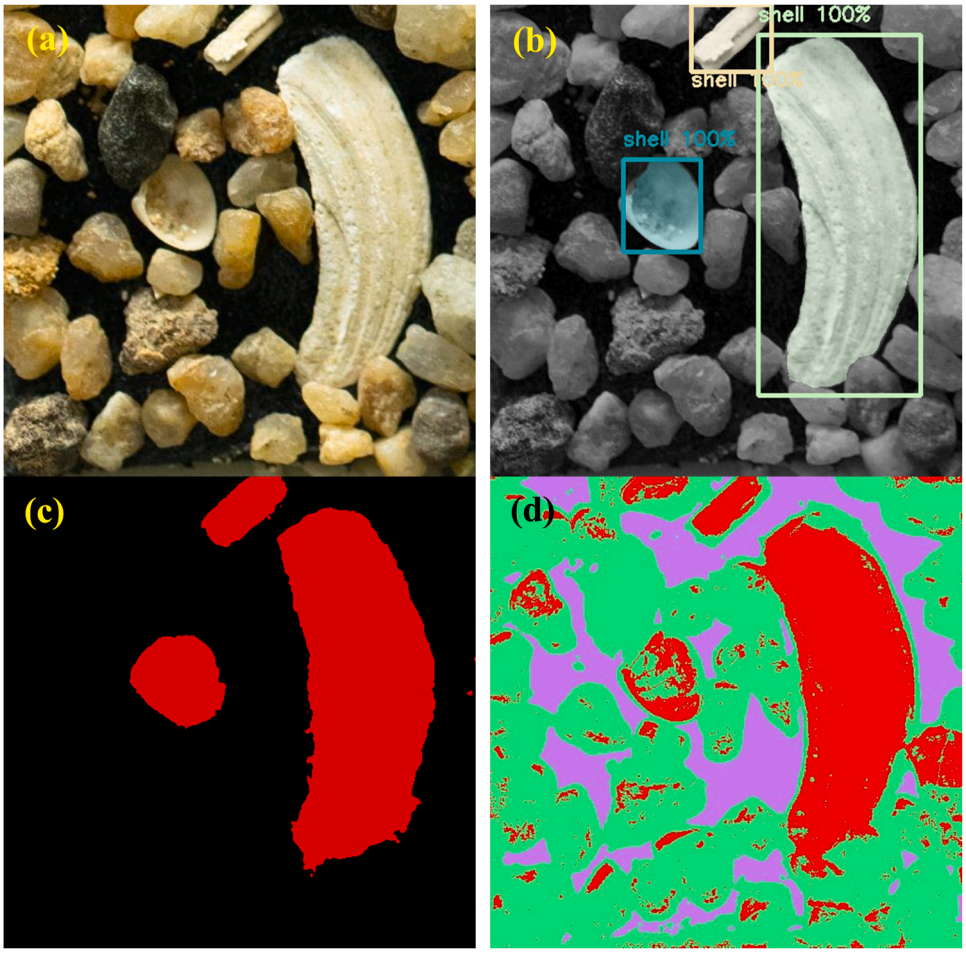

Fig. 6. Comparison of the segmentation results generated by (b) PointRend, (c) DeepLab V3, and (d) TWS to (a) the original image. (The reader is referred to the web version of this article for color in this figure.).

and background) and applied as a training collection for the classifier. In this study, “Gaussian blur,” “Sobel,” “Gaussian Difference,” “Hessian,” “variance,” “entropy,” and “membrane detectors” were selected as training features to reduce noise in the image, indicate object boundaries and corners, recognize object texture, and localize membranous structures. Detailed descriptions of the filters can be found in the literature [34,37]. Then, a fast random forest (RF) algorithm [38] was applied as a classifier based on the training set. The RF method is a simple, flexible, and efficient machine learning method that uses a subset of randomly selected training variables to generate multiple decision trees [39]. After training the RF classifier, the images of the test group were segmented into classified images. The detailed network configuration of the three modules can be found in the relevant literature [32–34].

2.3. LOI test for seashell weight percentage measurements

The LOI test was conducted to estimate the weight percentage of the seashells. The sieved sea sand samples were placed in crucibles and dried at 105 °C for 24 h. After recording the dry mass, the sea sand samples were placed in an electric furnace and ignited at 1000 °C for 4 h. The samples were then weighed on an analytical balance with a precision of 0.01 g. The mass difference between the 105 °C drying and 1000 °C ignition was used as the mass of the seashells.

2.4. Particle size calculation

To the best of the authors’ knowledge, no other methods have been implemented to separate the seashells and measure their size distribution. Moreover, it is very time-consuming for a person to count seashells. Therefore, based on the segmentation results, we proposed a method to solve this problem. After training, the best algorithm was chosen based on validation results. Then, the output was a binary prediction result, with 0 being the background and 1 being the shell. Finally, a minimum circumscribed circle was applied to each shell mask. The diameter of the minimum circumscribed circle was adopted as the size of the seashell.

3. Results and discussion

3.1. Network results

For the deep learning algorithms PointRend and DeepLab v3 + , the code was implemented in Pytorch, and training was performed on a single GPU (RTX2080). Both the PointRend and DeepLab used the ResNet50 as the backbone. As a widely accepted method to improve accuracy, the initial parameters of PointRend and DeepLab were loaded from a pre-trained model on the COCO dataset. To ensure sufficient optimization, training was completed in up to 20,000 iterations. After 20,000 steps, decreasing rate of the loss was negligible, thus it was believed the model converged. We employed a stochastic gradient descent optimizer with a batch size of 8 with a momentum $\mu_j = 0.9$. To ensure the stability of the training and to get a good model performance, the initial learning rate was set to 0.01, and then gradually reduced to 0.0001 as the training progressed. After convergence, the model was evaluated using images from all datasets with a subdivision step of 5.

Fig. 6 shows an example of the three methods to segment seashells from the sea sand and background. As can be seen in Fig. 6a, there are three seashells. The first shell at the top center is rod-like, while the second shell on the right side of the image is larger in size and shows a rough surface texture. The third shell in the center has a visible inner side and lots of dust attached to it. From Fig. 6b, we can see that PointRend has segmented the three shells quite accurately. The boundaries of the shells are also clearly and sharply defined. Difficult samples, such as semi-transparent quartz sand and blurry phase transitions, are not misrecognized. From Fig. 6c, we can see that the three shells are well recognized by the DeepLab v3 + model. Also, there is no misrecognition of sea sand particles. However, the object boundaries are fuzzy, and the masked areas are larger than the shells. In Fig. 6d, red represents the seashells, green represents the sea sand, and purple represents the background. In the TWS method, the background is well segmented, but many areas belonging to the sand particles are misrecognized as seashells. This is because the sea sand and shell regions share similar features at

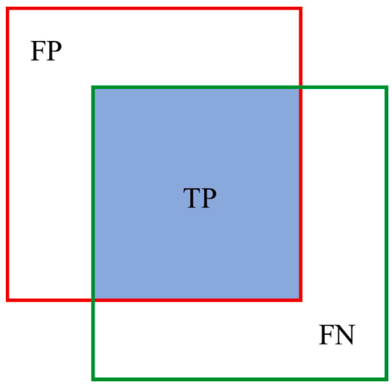

Fig. 7. Definition of IOU.

the pixel level.

To evaluate the prediction performance of the applied methods, we first used PA and IOU as evaluation metrics, which is popular used in the field of computer vision as the metric to evaluate the model performance. The PA is a straightforward concept representing the ratio of the number of correctly classified pixels of a shell to the total number of pixels assigned to the shell in the baseline image. The IOU is also a commonly used evaluation metric to measure the accuracy of an object detector for a particular dataset. Compared with PA, IOU is stricter to indicate the difference of models. As defined in Eq. 1, when the predicted bounding box overlaps significantly with the ground-truth bounding box, the IOU will have a higher score than less overlap.

$$IoU = \frac{TP}{(TP + FP + FN)} \tag{1}$$

where the true positive (TP) denotes the number of pixels correctly classified as shells. False positive (FP) denotes the number of pixels labeled as shells in the non-shell classes. False negative (FN) denotes the number of pixels where shells are incorrectly classified as background or sand pixels. Fig. 7 shows the definition of an IOU.

Table 2 shows the results of PA and IOU. The IOUs for the entire images and SS (small sand), MS (medium sand), and LS (large sand) groups are shown in Table 2. All IOU scores of the PointRend method are above 85. Moreover, the IOU score increased with increasing the size of the shells. This is probably because that although the distance between the camera and the samples is reduced proportionally during photographing small-sized sea sands, the quality of the images is reduced, and detailed information, such as the texture and pattern of the sand and the shells is inevitably lost. DeepLab v3 + is one of the most popular and generic algorithms in the field of segmentation. However, its overall IOU score is about 60.75, which is 27.13 lower than the IOU score of PointRend. In the SS group, the difference between these two methods is 28.51. In addition, the PA of DeepLab v3 + is 1.7 points lower than that of PointRend. However, as shown in Fig. 6, both the PointRend and DeepLab v3 + method detected the three shells well, indicating that the boundary quality of the PointRend method is crucial for a superior IOU result. Finally, the pixel-based segmentation method of TWS obtained the worst performance. As shown in Fig. 6d, segmentation using TWS could not sufficiently discriminate between sea sand and seashells. This is because they are similar in brightness, texture, and color, resulting in misinterpretation. Moreover, since TWS is a pixel-based method, it cannot segment grain boundaries clearly, but the other two models are able to do so.

To analyze the accuracy of the PointRend method, we applied a more detailed metric, the AP. The AP is calculated using the precision and recall (P–R) curve. Here, the precision represents the accuracy of prediction (Eq. 2), which is the percentage of correct predictions, and the recall represents how well the method can find all the positives (Eq. 3). The AP curve can be plotted in the following steps. First, all the predicted masks whose IOUs are higher than the image threshold are listed in order of their confidence level. Next, the precision and recall are calculated based on Eqs. 2 and 3 while gradually increasing the number of masks from the top of the list. Finally, a P–R curve can be plotted with precision against the recall. An example of a P–R curve is shown in Fig. 8, where the AP is defined as the area under the P–R curve. Typically, the precision decreases as the recall value increases. If the network is able to produce relatively high precision at a high recall value, the AP will be high. Thus, the AP is a criterion to evaluate the overall performance of a network.(Table 3)

$$Precision = \frac{TP}{TP + FP} \tag{2}$$

$$Recall = \frac{TP}{TP + FN} \tag{3}$$

In this study, AP means the average AP of over ten thresholds from 0.5 to 0.95, with an interval of 0.05. AP50 means a threshold of 0.5, which is a common level in the PASCAL VOC dataset. AP75 means a threshold of 0.75, which is a stricter criterion because more prediction instances are removed. APs, APm, and APl represent the AP values for small ($<32 \times 32$), medium ($>32 \times 32$, $<96 \times 96$), and large ($>96 \times 96$) regions, respectively. The results are shown in Table 4.

The scores for AP, AP50, and AP75 were 83.96, 94.90, and 94.62, respectively, which can be considered quite good results for segmentation tasks. The values of APm and APl are also satisfactory. On the contrary, APs show a low value of less than 80. First, small areas have little information, such as texture, color, and brightness. Thus, the network may recognize small sand particles as seashells due to little information. Moreover, labeling based on visual judgment is difficult for small shells. Errors in labeling can mislead the training process of the network. This increases the FP during prediction.

3.2. LOI and PointRend results

The weight percentage of the seashells was measured by LOI, and the area proportion calculated from the segmentation results is

Table 2
Segmentation accuracy of the three methods.

Metric	IOU	IOU on SS	IOU on MS	IOU on LS	PA
PointRend	87.88	86.50	87.17	91.21	99.29
DeepLab V3 +	60.75	57.99	61.98	63.90	97.57
TWS	23.55	17.71	29.38	29.88	91.92

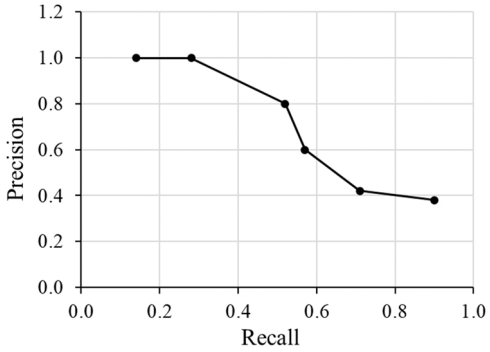

Fig. 8. The example of the P-R curve.

Table 3
Example of data for the P-R curve.

Recall	0.14	0.28	0.52	0.57	0.71	0.90
Precision	1.00	1.00	0.80	0.60	0.42	0.38
Confidence	1.00	0.98	0.95	0.94	0.92	0.91
IOU	0.87	0.76	0.78	0.91	0.74	0.88
Threshold	0.5	0.5	0.5	0.5	0.5	0.5

Table 4
AP result of PointRend on whole dataset.

Metric	AP	AP50	AP75	APs	APm	APl
PointRend	89.36	94.90	94.62	77.52	87.96	93.69

shown in Table 5. It can be seen that the content of shells increased with increasing the size of sand. It is worth noting that the two indices present different information and are difficult to compare directly. First, impurities other than seashells will also be calculated by the LOI method. Second, since the sea sand and seashells are irregularly shaped, images captured in 2D cannot be easily converted into volumetric information. Finally, natural materials, such as sea sand and especially seashells, have large variations in density, making accurate measurements difficult.

3.3. Particle analysis of seashells

The particle size distribution of the seashells is measured from the segmentation results. A well-trained model is used to generate a mask corresponding to each seashell. The size of the shells is defined as the diameter of the minimum circumscribed circle of the mask. Fig. 9 shows a plot of the distribution of seashells in 1 kg of the measured sea sand. A similar number of images were used to calculate the size distribution of shells in each sea sand group. However, since the image area of the group with smaller sand particles is smaller, and the sea sand layer on the adhesive plaster is thinner, the total weight of the sea sand measured in each group is not proportional to the actual ratio in the bulk sea sand. Therefore, the cumulative distribution of shells in 1 kg of sea sand is calculated by the following method.

$$\mathrm{Q}_s^{1kg} = \sum_{i=1}^{s} \Delta \mathrm{Q}_i^{1kg} \tag{4}$$

where $\mathrm{Q}_i^{1kg}$is the total amount of shells smaller than the size ofx_s, and $\Delta \mathrm{Q}_i^{1kg} = \mathrm{Q}^{1kg}(x_i) - \mathrm{Q}^{1kg}(x_{i-1})$is the increased number of shells in the size range of Δx_i. The sea sand sample was divided into three groups: SS, MS, and LS.

$$\Delta Q_i^{1kg} = \sum_{r=SS,MS,LS} \Delta Q_{i,r}^{1kg} \tag{5}$$

where $\Delta Q_{i,r}^{1kg}$is the number of shells in each group of samples in the size range of Δx_i. $\Delta Q_{i,r}^{1kg}$can be calculated by the following equation:

$$\Delta Q_{i,r}^{1kg} = \Delta Q_{i,r}^{test} \frac{m_r^{1kg}}{m_r^{test}} \tag{6}$$

where $\Delta Q_{i,r}^{test}$is the number of shells calculated directly from the images, $m_r^{1kg}$is the mass of sea sand in each group in 1 kg of sea sand,

Table 5
Comparison between mass proportion and area proportion.

Group	Initial mass (g)	Dry mass (g)	Mass loss (g)	Mass of shell (g)	Mass proportion of LOI (%)	Area proportion (%)
LS	1000	985.96	30.44	69.18	6.92	5.66
MS	1000	991.42	18.62	42.32	4.23	2.02
SS	1000	993.7	13.88	31.55	3.15	1.82

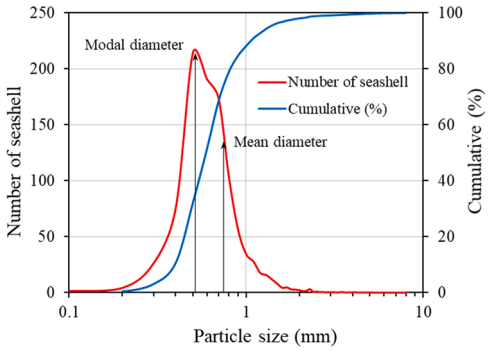

Fig. 9. Particle size distribution of the seashells.

and m_r^{test} is the mass of sea sand used for image capturing. Finally, the frequency distribution $q(x)$ is the differential of the accumulative frequency $dQ(x)/dx$.

As shown in Fig. 9, most seashell particles are smaller than 1 mm. As a result, the size of the seashells was smaller than that of the bulk sea sand, with a mean diameter of 0.747 mm and a modal diameter of 0.52 mm, showing a left-skewed distribution.

Two parameters, irregularity $I = d_{i\,\max}/d_{c\,\min}$ and roundness $C = \sqrt{4\pi A/P^2}$, were calculated from the segmented results to analyze the shape of the seashells, in which $d_{i\,\max}$, $d_{c\,\min}$, A, and P are the diameter of the maximum inscribed circle, the diameter of the minimum circumscribed circle, the area, and perimeter of the shells, respectively. Irregularity and roundness vary between 0 and 1, where 1 is a perfect circle. Fig. 10 shows that these two parameters present significant variations attributed to shellfish diversity and environmental impacts. Linear regression results show that irregularity and roundness tended to decrease with increasing the size of the seashell particles. This can be attributed to the fact that relatively intact shells have smaller dimensions in the thickness direction than the direction parallel to the surface of the shell. When the shells are crushed into small fragments, the thickness remains unchanged, but the surface area is reduced. Weathering also smoothens the sharp edges of the shells.

Given the above, artificially selected shells cannot usually represent them in nature due to their wider range of sizes, irregular shapes, and different types. Therefore, in studies on the effects of sea sand and shells on the properties of concrete, the shells need to be precisely characterized to avoid misleading results.

4. Conclusions

Without a comprehensive understanding of the characteristics of seashells, it is difficult to quantify their impact on concrete. To the best of the authors' knowledge, this is the first time to automatically recognize and analyze shells in sea sand using a machine learning algorithm based on computer vision. We compared the performance of three deep learning algorithms, PointRend, DeepLab v3 + , and Weka, in segmenting seashells from sea sand photos. The sea sand photos were taken with a digital camera to train the deep learning models and analyze the seashells. In order to avoid overlapping sea sand particles, we proposed a new image capturing method. The sea sand samples were divided into three sizes to guarantee sufficient resolution, even for small particles. The results demonstrated that shells of different shapes, sizes, and surface textures could be recognized and that the boundaries could be clearly defined by the PointRend algorithm. Therefore, the PointRend algorithm demonstrated the highest accuracy among the three algorithms in terms of IOU, PA, and AP. The particle size distribution of the seashells was calculated from the segmentation results. The size of the shells showed a left-skewed distribution with a mean diameter of 0.747 mm, which was smaller than the size of bulk sea sand. The irregularity and roundness of the shells were also analyzed. These two parameters showed significant variations, with the larger shells having more irregularity. This study demonstrates that deep learning is a powerful tool for analyzing sea sand with high accuracy and efficiency and without human intervention. This novel shell characterization method will contribute to further understanding of the impact of sea sand on the properties of concrete.

Declaration of Competing Interest

The authors declare that they have no known competing financial interests or personal relationships that could have appeared to influence the work reported in this paper.

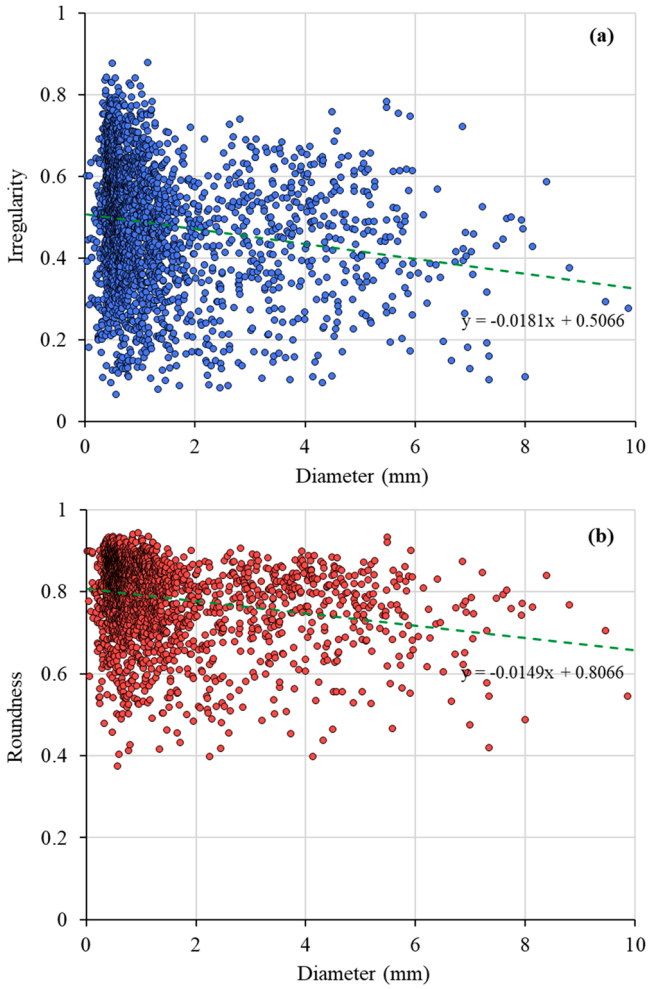

Fig. 10. (a) irregularity and (b) roundness of seashells against particle size.

Data Availability

Data will be made available on request.

Acknowledgments

This work was supported by the National Science Fund for Distinguished Young Scholars (No. 52025081), Shenzhen Science and Technology Program (No. KQTD20210811090112003), Shenzhen Science and Technology Program (GXWD20220817143919002), Shenzhen Science and Technology Program (No. RCYX20200714114525013). and Open Funding of State Key Laboratory of High Performance Civil Engineering Materials (2021CEM006).

Disclaimer

The authors declare that they have no known competing financial interests or personal relationships that could have influenced the work reported in this paper.

References

[1] Y. Zhao, X. Hu, C. Shi, Z. Zhang, D. Zhu, A review on seawater sea-sand concrete: Mixture proportion, hydration, microstructure and properties, Constr. Build. Mater. 295 (2021).
[2] A.C. Sankh, P.M. Biradar, S. Naghathan, M.B. Ishwargol, Recent trends in replacement of natural sand with different alternatives, Proc. Int. Conf. Adv. Eng. Technol. (2014) 59–66.
[3] J. Xiao, Q. Zhang, P. Zhang, L. Shen, C. Qiang, Mechanical behavior of concrete using seawater and sea-sand with recycled coarse aggregates, Struct. Concr. 20 (5) (2019) 1631–1643.

[4] A. Younis, U. Ebead, P. Suraneni, A. Nanni, Fresh and hardened properties of seawater-mixed concrete, Constr. Build. Mater. 190 (2018) 276–286.
[5] M. Etxeberria, J.M. Fernandez, J. Limeira, Secondary aggregates and seawater employment for sustainable concrete dyke blocks production: Case study, Constr. Build. Mater. 113 (2016) 586–595.
[6] N. Otsuki, A.K. Min, T. Nagata, C. Yi, Durability of seawater mixed concrete with different replacement ratio of BFS (Blast Furnace Slag) and FA (Fly Ash), J. Civ. Eng. Archit. 10 (2016) 568–580.
[7] M. Etxeberria, A. Gonzalez-Corominas, P. Pardo, Influence of seawater and blast furnace cement employment on recycled aggregate concretes' properties, Constr. Build. Mater. 115 (2016) 496–505.
[8] P. Sikora, K. Cendrowski, M. Abd Elrahman, S.-Y. Chung, E. Mijowska, D. Stephan, The effects of seawater on the hydration, microstructure and strength development of Portland cement pastes incorporating colloidal silica, Appl. Nanosci. (2019) 1–12.
[9] T. Dhondy, A. Remennikov, M. Neaz Sheikh, Properties and application of sea sand in sea sand–seawater concrete, J. Mater. Civ. Eng. 32 (12) (2020) 04020392.
[10] W. Liu, H. Cui, Z. Dong, F. Xing, H. Zhang, T.Y. Lo, Carbonation of concrete made with dredged marine sand and its effect on chloride binding, Constr. Build. Mater. 120 (2016) 1–9.
[11] J. Limeira, M. Etxeberria, L. Agulló, D. Molina, Mechanical and durability properties of concrete made with dredged marine sand, Constr. Build. Mater. 25 (11) (2011) 4165–4174.
[12] Y.T. Li, L. Zhou, M. Jiang, Y. Zhang, J. Shao, Experimental study on mechanical property of concrete based on seawater and sea sand, Adv. Mater. Res. (2013) 574–577. Trans Tech Publ.
[13] V. Badrinarayanan, A. Kendall, R. Cipolla, Segnet: A deep convolutional encoder-decoder architecture for image segmentation, IEEE Trans. Pattern Anal. Mach. Intell. 39 (12) (2017) 2481–2495.
[14] S. Grigorescu, B. Trasnea, T. Cocias, G. Macesanu, A survey of deep learning techniques for autonomous driving, J. Field Robot. 37 (3) (2020) 362–386.
[15] E. Yurtsever, J. Lambert, A. Carballo, K. Takeda, A survey of autonomous driving: Common practices and emerging technologies, IEEE Access 8 (2020) 58443–58469.
[16] G. Litjens, T. Kooi, B.E. Bejnordi, A.A.A. Setio, F. Ciompi, M. Ghafoorian, J.A. Van Der Laak, B. Van Ginneken, C.I. Sánchez, A survey on deep learning in medical image analysis, Med. Image Anal. 42 (2017) 60–88.
[17] K. Suzuki, Overview of deep learning in medical imaging, Radiol. Phys. Technol. 10 (3) (2017) 257–273.
[18] G. Guo, N. Zhang, A survey on deep learning based face recognition, Comput. Vis. Image Underst. 189 (2019), 102805.
[19] G. Yang, W. Feng, J. Jin, Q. Lei, X. Li, G. Gui, W. Wang, Face mask recognition system with YOLOV5 based on image recognition, 2020 IEEE 6th International Conference on Computer and Communications (ICCC), IEEE, 2020, pp. 1398–1404.
[20] A. Campbell, A. Both, Q.C. Sun, Detecting and mapping traffic signs from Google Street View images using deep learning and GIS, Comput. Environ. Urban Syst. 77 (2019), 101350.
[21] Y.-J. Cha, W. Choi, O. Büyüköztürk, Deep learning-based crack damage detection using convolutional neural networks, Comput. Aided Civ. Infrastruct. Eng. 32 (5) (2017) 361–378.
[22] H. Qian, P. Zhang, S. Ji, S. Cao, Y. Xu, Improving representation consistency with pairwise loss for masked face recognition, Proc. IEEE CVF Int. Conf. Comput. Vis. (2021) 1462–1467.
[23] Y.J. Cha, W. Choi, O. Büyüköztürk, Deep learning-based crack damage detection using convolutional neural networks, Comput. Civ. Infrastruct. Eng. 32 (5) (2017) 361–378.
[24] K. Jang, N. Kim, Y.-K. An, Deep learning–based autonomous concrete crack evaluation through hybrid image scanning, Struct. Health Monit. 18 (5–6) (2019) 1722–1737.
[25] S.E. Park, S.-H. Eem, H. Jeon, Concrete crack detection and quantification using deep learning and structured light, Constr. Build. Mater. 252 (2020), 119096.
[26] L. Minfei, G. Yidong, C. Ze, W. Zhi, S. Erik, Š. Branko, Microstructure-informed deep convolutional neural network for predicting short-term creep modulus of cement paste, Cem. Concr. Res. 152 (2022).
[27] J. Lin, Y. Liu, H. Sui, K. Sagoe-Crentsil, W. Duan, Microstructure of graphene oxide–silica-reinforced OPC composites: Image-based characterization and nano-identification through deep learning, Cem. Concr. Res. 154 (2022).
[28] H. Qian, Y. Li, J. Yang, L. Xie, K.H. Tan, Image-based microstructure classification of mortar and paste using convolutional neural networks and transfer learning, Cem. Concr. Compos. 129 (2022).
[29] X. Fang, C. Wang, H. Li, X. Wang, S. Zhang, X. Luo, H. Jia, Influence of mesoscopic pore characteristics on the splitting-tensile strength of cellular concrete through deep-learning based image segmentation, Constr. Build. Mater. 315 (2022), 125335.
[30] H. Qian, Y. Li, J. Yang, L. Xie, K.H. Tan, Segmentation and analysis of cement particles in cement paste with deep learning, Cem. Concr. Compos. 136 (2023), 104819.
[31] Y. Song, Z. Huang, C. Shen, H. Shi, D.A. Lange, Deep learning-based automated image segmentation for concrete petrographic analysis, Cem. Concr. Res. 135 (2020).
[32] A. Kirillov, Y. Wu, K. He, R. Girshick, Pointrend: Image segmentation as rendering, Proc. IEEE CVF Conf. Comput. Vis. Pattern Recognit. (2020) 9799–9808.
[33] L.-C. Chen, Y. Zhu, G. Papandreou, F. Schroff, H. Adam, Encoder-decoder with atrous separable convolution for semantic image segmentation, Proc. Eur. Conf. Comput. Vis. ECCV (2018) 801–818.
[34] I. Arganda-Carreras, V. Kaynig, C. Rueden, K.W. Eliceiri, J. Schindelin, A. Cardona, H. Sebastian Seung, Trainable Weka Segmentation: a machine learning tool for microscopy pixel classification, Bioinformatics 33 (15) (2017) 2424–2426.
[35] J. Long, E. Shelhamer, T. Darrell, Fully convolutional networks for semantic segmentation, Proc. IEEE Conf. Comput. Vis. Pattern Recognit. (2015) 3431–3440.
[36] L.-C. Chen, G. Papandreou, F. Schroff, H. Adam, Rethinking atrous convolution for semantic image segmentation, arXiv Prepr. arXiv 1706 (2017) 05587.
[37] S.S. Bangaru, C. Wang, M. Hassan, H.W. Jeon, T. Ayiluri, Estimation of the degree of hydration of concrete through automated machine learning based microstructure analysis – A study on effect of image magnification, Adv. Eng. Inform. 42 (2019).
[38] L. Breiman, Random forests, Mach. Learn. 45 (1) (2001) 5–32.
[39] Q. Feng, J. Liu, J. Gong, UAV remote sensing for urban vegetation mapping using random forest and texture analysis, Remote Sens. 7 (1) (2015) 1074–1094.